Acta Pharmaceutica Sinica B 2025;15(7):3708−3724

Chinese Pharmaceutical Association
Institute of Materia Medica, Chinese Academy of Medical Sciences

Acta Pharmaceutica Sinica B

www.elsevier.com/locate/apsb
www.sciencedirect.com

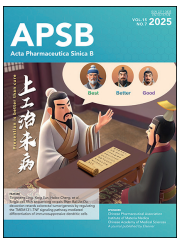

ORIGINAL ARTICLE

CMD-OPT model enables the discovery of a potent and selective RIPK2 inhibitor as preclinical candidate for the treatment of acute liver injury

Yong Chen[a,b,†], Xue Yuan[a,†], Wei Yan[a,†], Yurong Zou[a,†], Haoche Wei[a], Yuhan Wei[a], Minghai Tang[a], Yulian Chen[a], Ziyan Ma[a], Tao Yang[a], Kongjun Liu[a], Baojian Xiong[a], Xiuying Hu[b,*], Jianhong Yang[a,*], Lijuan Chen[a,c,*]

[a]*State Key Laboratory of Biotherapy, Collaborative Innovation Center of Biotherapy, West China Hospital, Sichuan University, Chengdu 610041, China*
[b]*Innovation Center of Nursing Research and Nursing Key Laboratory of Sichuan Province, West China Hospital, Sichuan University/West China School of Nursing, Sichuan University, Chengdu 610041, China*
[c]*Chengdu Zenitar Biomedical Technology Co., Ltd., Chengdu 610212, China*

Received 30 October 2024; received in revised form 14 April 2025; accepted 16 April 2025

KEY WORDS

CMD-OPT;
Acute liver injury;
RIPK2 inhibitors;
Anti-inflammatory;
Drug discovery;
Co-crystal;
Candidate;
Kinase specificity

Abstract Acute liver injury (ALI) serves as a critical precursor and major etiological factor in the progression and ultimate manifestation of various hepatic disorders. The prevention and treatment of ALI is still a serious global challenge. Given the limited therapeutic options for ALI, exploring novel targeted therapeutic agents becomes imperative. The potential therapeutic efficacy of inhibiting RIPK2 is highlighted, as it may provide significant benefits by attenuating the MAPK pathway and NF-κB signaling. Herein, we propose a CMD-OPT model, a two-stage molecular optimization tool for the rapid discovery of RIPK2 inhibitors with optimal properties. Compound **RP20**, which targets the ATP binding site, demonstrated excellent kinase specificity, ideal oral pharmacokinetics, and superior therapeutic effects in a model of APAP-induced ALI, positioning **RP20** as a promising preclinical candidate. This marks

*Corresponding authors.
E-mail addresses: huxiuying@scu.edu.cn (Xiuying Hu), yjh1988@scu.edu.cn (Jianhong Yang), chenlijuan125@163.com (Lijuan Chen).
[†]These authors made equal contributions to this work.
Peer review under the responsibility of Chinese Pharmaceutical Association and Institute of Materia Medica, Chinese Academy of Medical Sciences.

https://doi.org/10.1016/j.apsb.2025.05.003

the first application of RIPK2 inhibitors in ALI treatment, opening a novel therapeutic pathway for clinical applications. These results highlight the efficacy of the CMD-OPT model in producing lead compounds from known active molecules, showcasing its significant potential in drug discovery.

1. Introduction

Acetaminophen (APAP) is a frequently employed non-steroidal anti-inflammatory drug and is a predominant initiator of drug-induced liver injury (DILI), responsible for nearly half of acute liver failure (ALF) cases in both Europe and the US[1-5]. Excessive hepatic metabolism of APAP produces the toxic metabolite *N*-acetyl-*p*-benzoquinone imine (NAPQI), thereby leading to hepatocellular damage[6-9]. Although *N*-acetylcysteine (NAC) is the sole FDA-approved treatment agent for APAP-induced ALI, its effectiveness is limited by its short duration and low bioavailability[10,11]. Given the lack of effective treatments for ALI, the discovery of new targeted therapeutic agents is critical. NAPQI-induced liver cell injury releases pro-inflammatory substances like TNF-α, IL-1β, and IL-6, which attract macrophages and neutrophils, worsening inflammation and ALI[12,13]. Targeting key pathways such as MAPK and NF-κB signaling is a promising strategy for mitigating APAP-induced ALI[14,15]. Receptor-interacting serine−threonine kinase 2 (RIPK2), activated in conjunction with nucleotide-binding oligomerization domain (NOD1 or NOD2), initiates NF-κB and MAPK pathways. This activation subsequently recruits downstream kinases (TAK1, IKKα, IKKβ, and IKKξ), triggering immune-related signaling, inflammation, and autophagy[16-18]. Inhibition of RIPK2, renowned for its involvement in inflammation and cell apoptosis, may confer therapeutic benefits by suppressing JNK activation within the MAPK pathway[19]. Additionally, modulating NF-κB signaling through RIPK2 inhibition highlights its potential as a therapeutic target in the treatment of ALI.

Recently, a multitude of RIPK2 inhibitors have been unveiled, categorized as either non-selective or selective ATP-competitive compounds[20-29] (Fig. 1). **GSK2983559** (GSK), notably a first-in-class RIPK2 inhibitor, advanced to a clinical phase I trial for inflammatory bowel diseases (IBD). Unfortunately, its development was discontinued due to preclinical toxicity and narrower safety thresholds (NCT03358407). Concurrently, OD101, with undisclosed structural details, entered phase I clinical trials in 2023 as a novel therapeutic agent for IBD. Additionally, AC-101, also lacking structural information, commenced its initial dosing phase in Australia in 2023. These developments highlight the ongoing exploration of RIPK2 inhibition as a potential avenue for the management of IBD.

In this study, we present a CMD-OPT (constrained molecular design-optimization), a two-stage molecular optimization tool leveraging a known active lead compound aimed at discovering

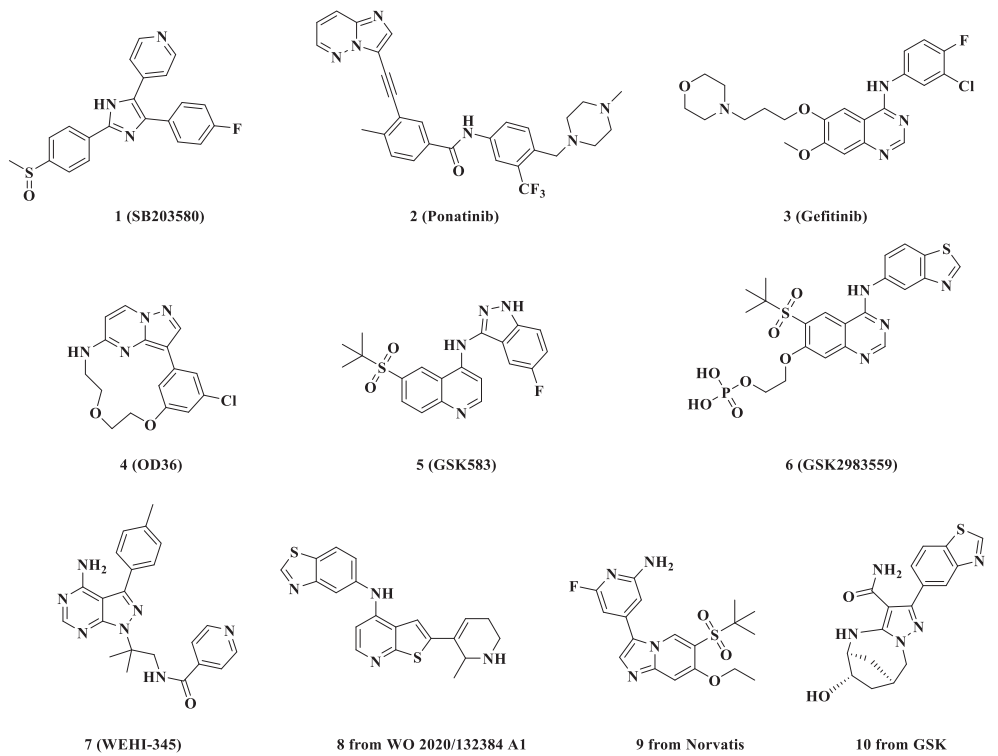

Figure 1 Representative RIPK2 inhibitors.

potent RIPK2 inhibitors. Next, we explore the identification of **RP20**, a highly potent and selective RIPK2 inhibitor that specifically targets the ATP-binding pocket. Notably, compound **RP20** demonstrated remarkable potency, kinase selectivity, a favorable safety margin, and advantageous oral pharmacokinetic properties. Significantly, in an APAP-induced ALI model, **RP20** exhibited superior *in vivo* efficacy compared to **GSK29835559** and NAC.

2. Results

2.1. Establishment of the CMD-OPT model

The utilization of molecular generation models in pharmaceutical design is progressively gaining prominence. By integrating with optimization algorithms or reinforcement learning approaches, researchers can sample molecules with desired target properties[30,31]. For instance, the advanced multi-objective optimization model MCMG[32] leverages knowledge distillation, conditional transformer (c-transformer), and reinforcement learning (RL) to generate molecules that satisfy multiple constraints. However, such models require task-specific data and training from scratch, limiting their applicability and adaptability. In contrast, search-based algorithms like MolSearch[33] heavily rely on predefined transformation rules. The efficacy of these algorithms depends on the quality and scope of the rules, which can constrain their ability to thoroughly explore the chemical space. To address these limitations, we present an accessible, two-stage molecular optimization model based on a transformer encoder-decoder framework. The model divides the optimization process into framework hopping and property refinement stages, enhancing chemical space exploration. It utilizes 2D fingerprint similarity and 3D shape pharmacophore similarity as constraints, alongside properties that need to be optimized, including whether they should be increased or decreased. On the evaluation metrics of MOSES[34], our model demonstrated capabilities comparable to the current state-of-the-art techniques. It also showed excellent performance in generating molecule sets that meet the target conditions in the test set sampling, as detailed in Supporting Information Fig. S1 and Supporting Information Table S1.

During the development of RIPK2 inhibitors, we selected the lead compound **GSK2983559** as the starting point for our research (Fig. 2). By systematically pruning the side chains of **GSK2983559** using the BRICS algorithm[35], we generated a broader set of data inputs for the first stage of scaffold hopping in our model. For each input, we sampled 1000 epochs and selected the top 100 molecules. In total, we obtained 684 non-redundant potential scaffold hopping-derived molecules. From each cluster based on scaffold clustering, we selected the highest-scoring molecule through docking, with the results shown in Supporting Information Fig. S2. These molecules share common scaffolds found in kinase inhibitors, with clusters 5, 7, 8, and 10 ranking among the top-scoring molecules, all with scores exceeding −10.

To enhance the success rate of the development process, we hypothesized that the synthesized molecules should incorporate scaffolds with desired attributes. Based on this assumption, we selected the highest-scoring molecules from clusters 8 and 10 as candidates for subsequent property optimization. For the scaffold of compound 8, our hypothesis posited that the introduction of methyl to the thiophene ring would create steric hindrance to the 4-tetrahydropyridine moiety, potentially increasing the synthesis difficulty. Additionally, its hydrophobic nature could interfere with NH−H bonding with water molecules, as shown in Supporting Information Fig. S3. Therefore, during the property optimization phase, we simplified the methyl group by directly using pyrimidine-thiophene as the scaffold. However, for molecules with scaffold 10, we found that patent restrictions significantly impeded direct development, thus designating them for future research.

Moreover, the molecules optimized from compound 8 featured a pyrimidine-thiophene scaffold demonstrating novelty, as this skeleton had not been previously reported in RIPK2 series inhibitors. Although the lead compound and compound 8 are distinct entities, issues such as high clinical clearance rates and low exposure levels have been observed with the lead compound. Properties associated with compound 8, such as hepatic microsomal stability, reduced clearance rates, and enhanced $T_{1/2}$ values, indicate the need for further optimization. In the second round of optimization, we utilized properties predicted by the ADMET Lab 3.0 API[36] as constraints in molecular generation, specifically targeting CL reduction, $T_{1/2}$ increase, increased stability in human liver microsomes (HLM), and QED increase. Following the principle of optimizing the synthesis route, we screened the top 30 most promising molecules based on docking scores and visual inspection, as detailed in Fig. S3. Ultimately, we selected 20 molecules (**RS1-20**, Schemes 1 and 2) for synthesis and evaluation of RIPK2 activities and HLM stability.

2.2. Retrieval of potent RIPK2 inhibitors

For compounds **RS1**, **RS4**, **RS5**, **RS13**, **RS17**, and **RS18**, which demonstrated potent inhibitory activities against RIPK2 kinase and stable HLM stability, plasma concentrations were determined following oral gavage at 10 mg/kg in BALB/c mice. Compound **RS5** not only exhibited a nanomolar IC_{50} value but also achieved adequate plasma drug exposure following oral gavage. However, the pharmacokinetics (PK) of **RS5** is inferior to that of **GSK2983559** (Table 1). Using CMD-OPT model, we successfully obtained a set of potent RIPK2 inhibitors featuring a novel scaffold. However, further optimization to improve PK is necessary. Introducing a halogen is a common strategy to improve pharmacokinetics of lead compounds. Building on the preceding results, we meticulously designed and synthesized a set of novel putative RIPK2 inhibitors (**RP1-29**) with a fluorine atom at the C-6 position of benzothiazole, categorically falling into three distinct types. The synthetic paradigm, illustrated in Schemes 3 and 4, involved the preparation of key intermediates **RP1**, **RP8**, and **RP16** through a three-step synthetic route initiated from the starting material **11**. Subsequent nucleophilic addition reactions with various anhydrides or isocyanates culminated in the synthesis of the final products, namely **RP2-7**, **RP9-15**, and **RP17−29**, respectively.

As expected, most of the compounds exhibited favorable metabolic stability in the HLM assay. Meanwhile, all compounds exhibited potent inhibitory activities against RIPK2 (IC_{50}: 6−17 nmol/L) and notable selectivity against RIPK1, comparable to **GSK2983559** (Table 2). Following plasma exposure assessments for selected compounds (Supporting Information Table S2), compounds **RP9**, **RP10**, **RP12**, **RP18**, **RP20**, and **RP21** were further evaluated for their pharmacokinetic properties through both intravenous (i.v.) injection and oral administration at the dosage of 10 mg/kg (Supporting Information Table S3). Although the 6-position of the phenyl ring may not be a major metabolic site, the introduction of a highly electronegative fluorine atom can

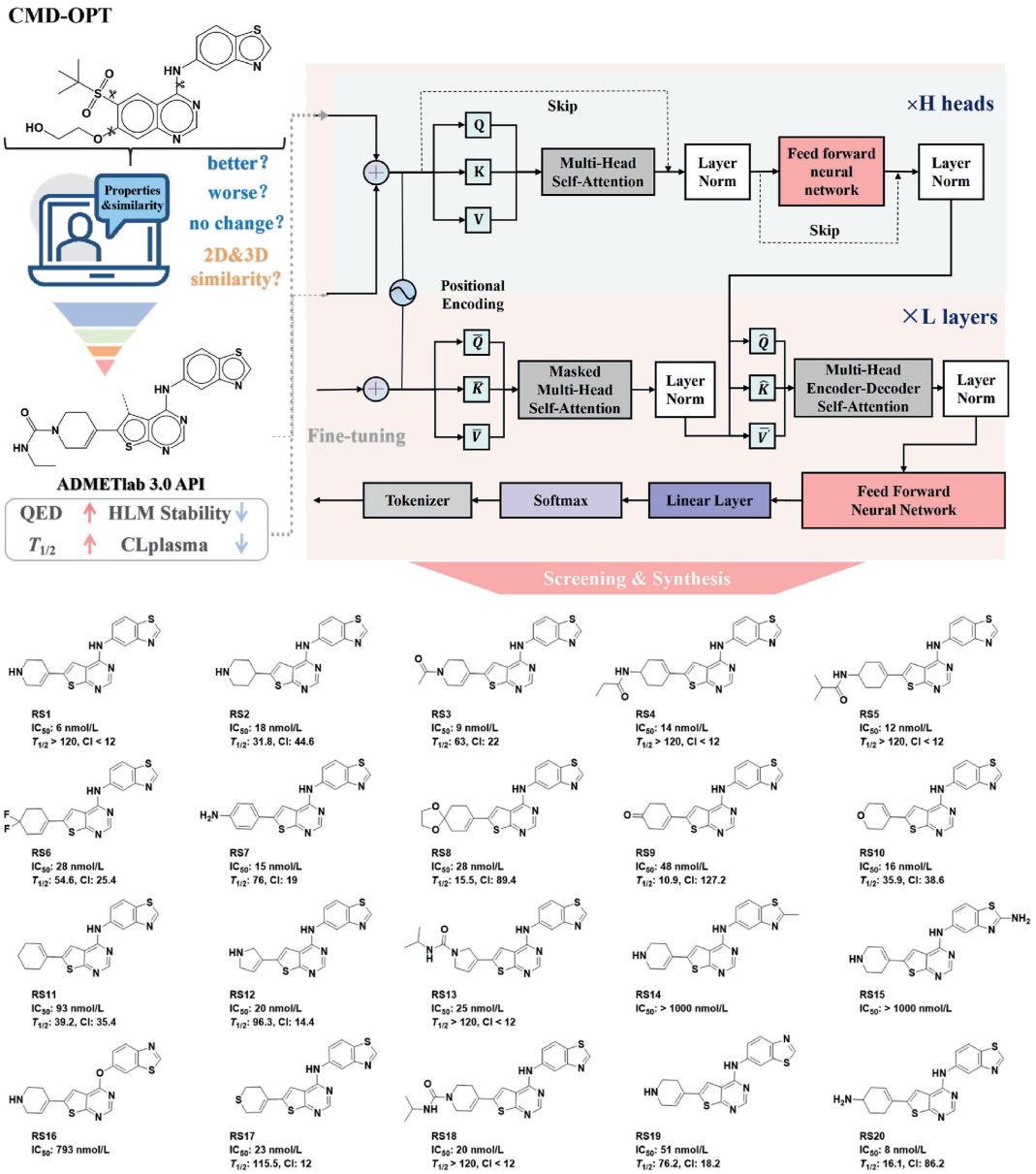

Figure 2 Framework and schematic workflow for designing RIPK2 inhibitors using CMD-OPT model.

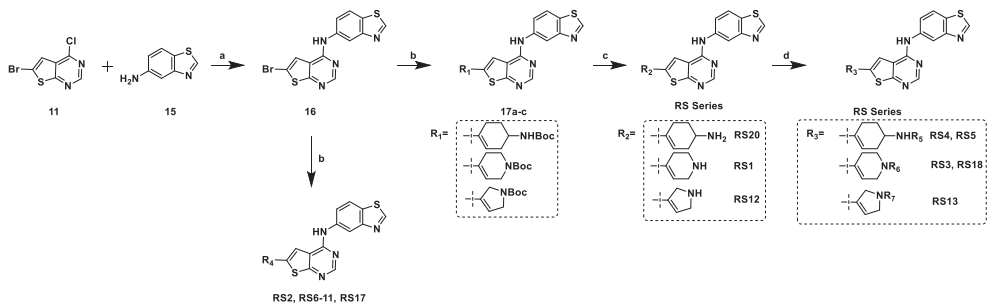

Scheme 1 Synthetic approach to **RS1-13**, **17**, **18**, **20**. (a) *p*-TSA, IPA, 80 °C; (b) The corresponding borate ester or borate, K_2CO_3, $PdCl_2$(dppf), Dioxane/EtOH/H_2O, 80 °C; (c) TFA, DCM, rt; KOH, H_2O; (d) The corresponding anhydride or isocyanate, DCM/MeOH, rt.

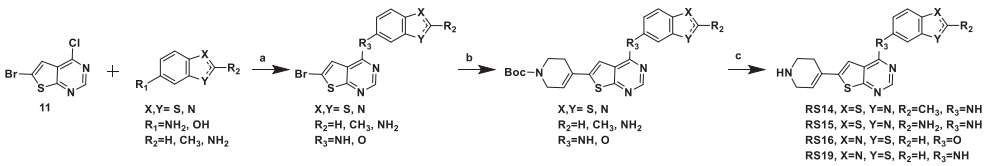

Scheme 2 Synthetic approach to **RS14**, **15**, **16**, **19**. (a) *p*-TSA, IPA, 80 °C or NaOH, H_2O, 80 °C; (b) 286961-14-6, K_2CO_3, $PdCl_2$(dppf), Dioxane/EtOH/H_2O, 80 °C; (c) TFA, DCM, rt; KOH, H_2O.

Table 1 IC_{50} values against RIPK2 and plasma concentration of optimized compounds.

Compound	RIPK2 IC_{50}, nmol/L[a]	Plasma concentration, ng/mL[b]		
		0.5 h	2 h	6 h
RS1	6	304.69 ± 133.17	432.94 ± 293.48	171.81 ± 103.31
RS4	14	452.68 ± 199.5	84.54 ± 34.7	29.19 ± 11.76
RS5	12	958.53 ± 185.52	125.23 ± 23.24	8.76 ± 2.74
RS13	25	79.54 ± 4.65	47.7 ± 11.3	52.8 ± 30.79
RS17	23	8.48 ± 5.45	4.39 ± 0.83	5.21 ± 0.23
RS18	20	5.07 ± 1.95	0.82 ± 0.14	0.42 ± 0.06
GSK2983559	7	1154 ± 125	145 ± 42	21 ± 11

[a]The IC_{50} values represent averages derived from dose–response curves obtained in three independent examinations.
[b]Dosage: 10 mg/kg *p.o.*; BALB/c mice, $n = 3$.

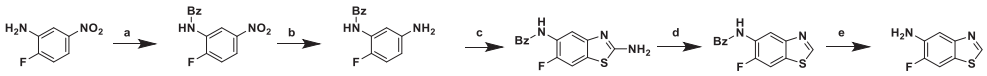

Scheme 3 Synthetic approach of intermediate **12**. (a) BzCl, CH_3CN, 50 °C; (b) Fe, NH_4Cl, MeOH/H_2O, 65 °C; (c) Br_2, KSCN, CH_3COOH, rt; (d) *tert*-Butyl nitrite, THF, 65 °C; (e) 70% H_2SO_4, 100 °C.

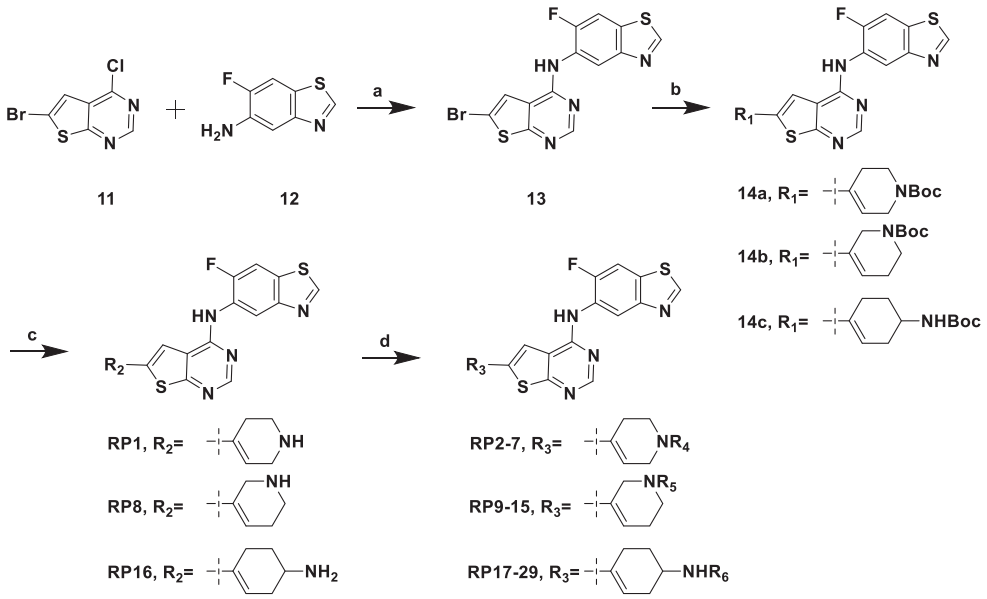

Scheme 4 Synthetic approach to **RP1-29**. Reagents and conditions: (a) *p*-TSA, IPA, 80 °C; (b) The corresponding borate ester or borate, K_2CO_3, $PdCl_2$ (dppf), Dioxane/EtOH/H_2O, 80 °C; (c) TFA, DCM, rt; KOH, H_2O; (d) The corresponding anhydride or isocyanate, DCM/MeOH, rt.

Table 2 The IC_{50} values against RIPK2, percent inhibition relative to control for RIPK1, and metabolic stability profiles of compounds **RP1-29**.

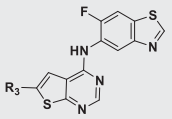

Compound	R_3	RIPK2	RIPK1	$T_{1/2}$ (min)	CL (mL/min/g·protein)
		IC_{50}, nmol/L[a]	Percentage%@1 μmol/L[b]		
RP1		9	99 ± 2	>120	<12
RP2	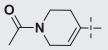	11	107 ± 4	115.5	12
RP3	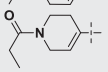	14	106 ± 6	99.0	14
RP4	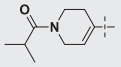	6	100 ± 5	>120	<12
RP5	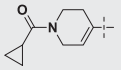	11	105 ± 2	>120	<12
RP6	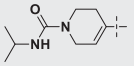	10	100 ± 4	>120	<12
RP7	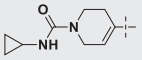	12	98 ± 2	>120	<12
RP8		9	95 ± 1	>120	<12
RP9		8	103 ± 0	>120	<12
RP10	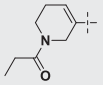	11	99 ± 1	>120	<12
RP11	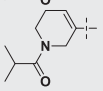	9	101 ± 4	>120	<12
RP12	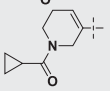	8	95 ± 2	>120	<12
RP13	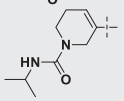	9	97 ± 3	>120	<12
RP14	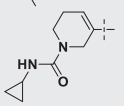	11	100 ± 3	>120	<12
RP15	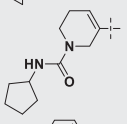	10	96 ± 2	>120	<12
RP16	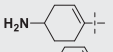	8	110 ± 5	>120	<12
RP17	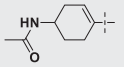	14	108 ± 1	>120	<12
RP18	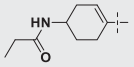	12	105 ± 3	>120	<12
RP19	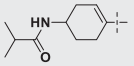	12	99 ± 2	53.3	26
RP20	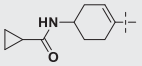	13	97 ± 2	>120	<12

(*continued on next page*)

Table 2 (*continued*)

Compound	R_3	RIPK2	RIPK1	$T_{1/2}$ (min)	CL (mL/min/g·protein)
		IC_{50}, nmol/L[a]	Percentage%@1 μmol/L[b]		
RP21	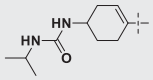	11	107 ± 3	>120	<12
RP22	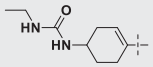	10	95 ± 2	>120	<12
RP23	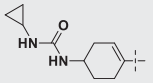	10	99 ± 2	>120	<12
RP24	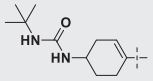	9	105 ± 6	>120	<12
RP25	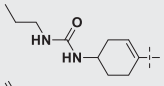	11	97 ± 1	>120	<12
RP26	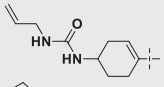	7	102 ± 3	>120	<12
RP27	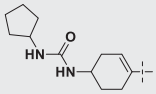	10	94 ± 1	>120	<12
RP28	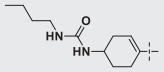	8	109 ± 4	>120	<12
RP29	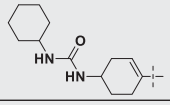	17	96 ± 2	>120	<12

[a]The IC_{50} values represent averages derived from dose−response curves of at least two examinations.
[b]The average percentage indicates the active RIPK1 activity in the duplicated tests. The activity was determined relative to control, using a consistent concentration of 1 mmol/L across all experiments.

alter the distribution of the electron cloud, thereby affecting the polarity of the molecule. This change can influence the ADME properties of the drug and potentially improve membrane permeability. Among them, **RP20** stood out with an IC_{50} value of 13 nmol/L against RIPK2 and exhibited at least 2000-fold selectivity over RIPK1 (Fig. 5A, Table 3).

2.3. *Pharmacokinetic characteristics of **RP20***

As shown in Table 4, **RP20** demonstrated exceptional oral exposure with an AUC value of 41021 ng/mL·h, an extended $T_{1/2}$ of 3.95 h, and a remarkable bioavailability of 95.9% at 10 mg/kg *via* oral administration, surpassing that of **GSK2983559**. Furthermore, a linear AUC-dosage relationship was observed in mice (Supporting Information Table S4), and **RP20** exhibited favorable PK characteristics in SD rats. Consequently, **RP20** was identified as a potent RIPK2 inhibitor for further assessment, effectively addressing major pharmacokinetic deficiencies associated with **GSK2983559** (Supporting Information Table S5).

Table 3 IC_{50} values for RIPK2 and RIPK1 of compound **RP20** and **GSK2983559**[a].

Compound	Structure	RIPK2	RIPK1
		IC_{50}, nmol/L	IC_{50}, μmol/L
RP20	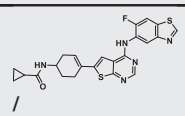	13	>30
GSK2983559	/	7	>30

[a]The IC_{50} values represent averages derived from dose−response curves obtained in two independent examinations.

2.4. ***RP20** delays NF-κB activation and RIPK2 ubiquitylation*

Upon NOD stimulation, RIPK2 undergoes significant ubiquitination. This process is essential for recruiting the linear ubiquitination assembly complex (LUBAC) to the signaling complex, thereby promoting effective downstream signaling[37]. Consequently, we aimed to investigate the impact of RIPK2 on its own ubiquitination process. Inhibition of RIPK2 kinase activity using **RP20** markedly suppressed RIPK2 ubiquitylation induced by MDP in a concentration-dependent fashion (Fig. 3A). Subsequently, THP-1 cells and BMDMs were stimulated with L18-MDP, and lysates were collected at specific time points post-stimulation (Fig. 3B and C). Western blotting analysis indicated that **RP20** delayed, rather than completely inhibited, the phosphorylation of p65, p38, and JNK. These proteins serve as molecular markers for the activation of NF-κB and MAPK signaling pathways following RIPK2 activation.

2.5. *The X-ray co-crystallographic structure of RIPK2 bound to **RP20***

To investigate the structural basis of RIPK2 inhibitor interactions, we successfully resolved the co-crystallographic structure of the

Table 4 Pharmacokinetic properties of compound **RP20** and **GSK2983559** in BALB/c mice[a].

Compound	Adm.	C_{max} (ng/mL)	$T_{1/2}$ (h)	V_z (L/kg)	Cl (mL/min/kg)	$AUC_{(0-t)}$ (ng/mL·h)	F (%)
RP20	i.v.	6034 ± 588	3.54 ± 1.06	1.19 ± 0.15	0.25 ± 0.07	42791 ± 11262	/
	p.o.	3648 ± 492	3.95 ± 0.61	/	/	41021 ± 3137	95.9
GSK2983559	i.v.	5675 ± 521	2.42 ± 0.86	9.46 ± 4.13	2.66 ± 0.19	3778 ± 255	/
	p.o.	2618 ± 413	2.74 ± 0.25	/	/	3123 ± 1059	82.7

[a]The data represent the mean values obtained from four independent determinations.

RIPK2 kinase domain in complex with **RP20** at a resolution of 2.26 Å (Supporting Information Table S6). As illustrated in Fig. 4A−D, the pyrimidine moiety interacted with the backbone amide NH of Met98, while the thiazole moiety engaged an interaction with Asp164. Moreover, the crystal structure indicates that the NH linking pyrimidine and benzene of **RP20**, along with the carbonyl group of the amide, can participate in hydrogen bonding interactions with water molecules. This interaction potentially aids in the entropy effects during molecular binding. Moreover, fragment molecular orbital (FMO) analysis revealed notable distinctions that may not be discernible through visual examination alone, such as with Glu105 and Glu66, which suggested that **RP20** can form robust and stable interactions with pocket residues (Fig. 4E).

2.6. *Kinase selectivity and safety assessment of **RP20***

Typically, ATP-competitive kinase inhibitors face selectivity challenges, including potential non-target toxicity. **RP20** underwent thorough profiling against a set of 373 human-derived kinases at 1 μmol/L in Eurofins Discovery to evaluate its selectivity profile. As depicted in Fig. 5B and detailed in Supporting Information Table S7, **RP20** demonstrated minimal inhibition against the majority of these kinases except for RIPK2. The selectivity fold was notably greater than 15, particularly in comparison to DDR1 kinase. Subsequently, the *in vitro* safety assessment of **RP20** was meticulously executed utilizing the Safety47™ panel from Discover X Corp., as elucidated in Supporting Information Table S8. Notably, **RP20** successfully passed all rigorous tests conducted, thereby affirming its praiseworthy safety profile. Concurrently, a comprehensive safety evaluation of **RP20** in SD rats was conducted through a sequential 28-day *in vivo* study, with an oral dose of 100 mg/kg. The comprehensive insights presented in Supporting Information Figs. S4−S7 unequivocally validate **RP20** as a secure preclinical candidate.

2.7. *In vivo effects of **RP20** in MDP-induced peritonitis and APAP-induced ALI model*

Founded on its potent activity against RIPK2, coupled with favorable pharmacokinetics and oral safety profile, **RP20** advanced to *in vivo* efficacy evaluation in MDP-induced

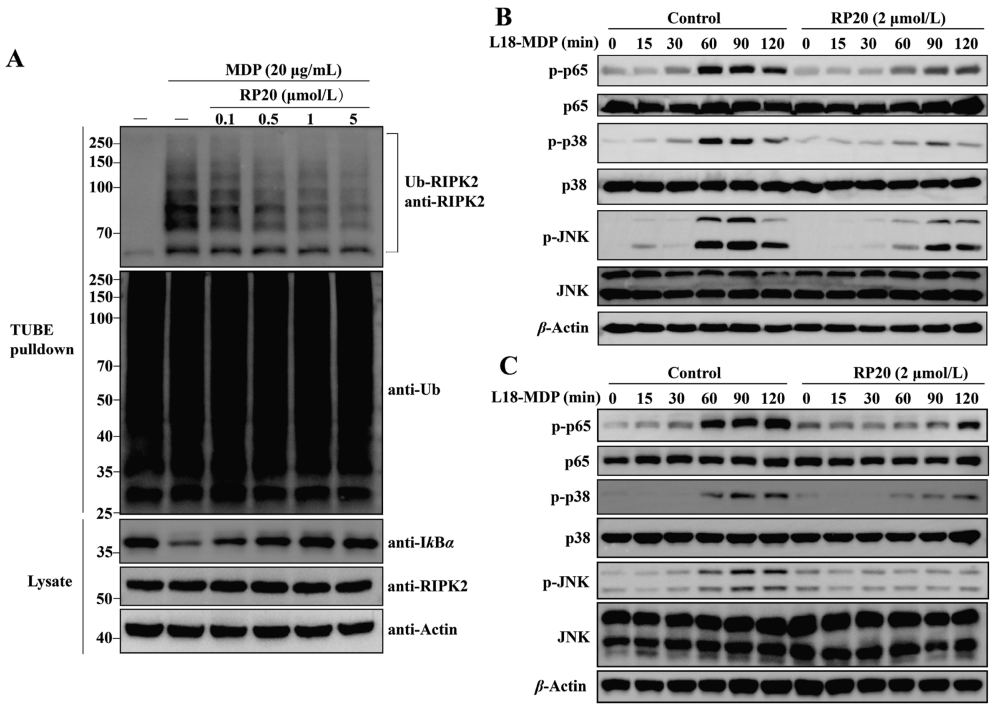

Figure 3 Inhibition of RIPK2 activity delays NF-κB activation and RIPK2 ubiquitination. (A) THP-1 cells were either untreated or pre-treated with **RP20** and then stimulated with MDP for specified durations. Ubiquitin conjugates were purified using TUBEs, and both lysates and pull-down samples were subjected to WB analysis using the specified antibodies. (B) THP-1 cells were treated with **RP20** (2 μmol/L) or left untreated for 0.5 h before stimulation with L18-MDP (200 ng/mL). Cell lysates were harvested at indicated time points and analyzed by WB for p-p65, total p65, p-p38, total p38, p-JNK. (C) BMDMs were treated with **RP20** (2 μmol/L) or left untreated for 0.5 h prior to stimulation with L18-MDP (200 ng/mL). Cell lysates were harvested at specified time points and analyzed by WB for p-p65, total p65, p-p38, total p38, p-JNK ($n = 3$).

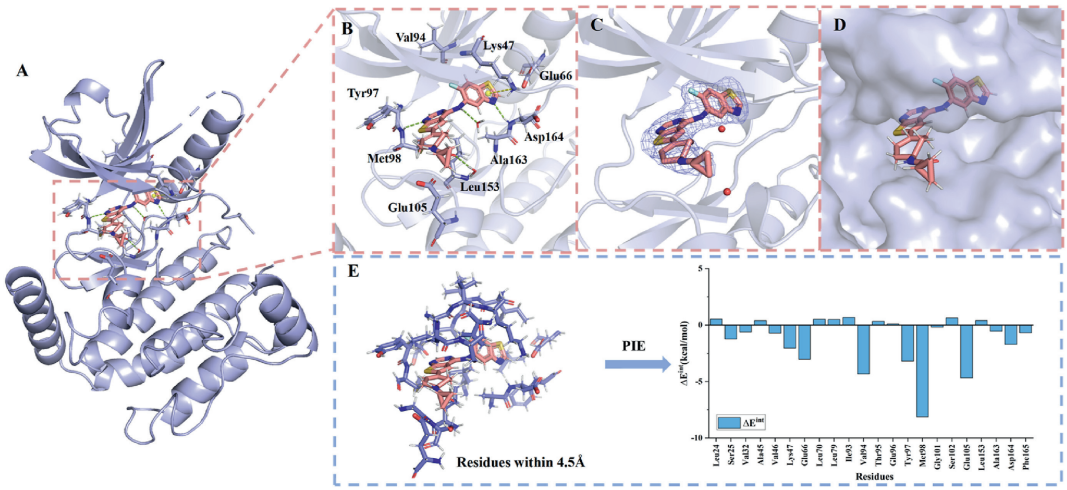

Figure 4 Cocrystal structure of **RP20** bound within the ATP binding pocket of RIPK2 kinase (PDB: 8X2O). (A) Overview of cocrystal structure of RIPK2 in complex with compound **RP20**. (B) Detailed depiction of the ATP binding pockets with surrounding key residues depicted as stick models. Hydrogen bonds are indicated by green dashed lines, and the cation−π interaction is denoted by yellow dashed line. (C) Density map of **RP20** within the binding site. (D) Protein surface of RIPK2 with the binding structure of **RP20**. (E) The Pair Interaction Energy (PIE) diagram for **RP20** was constructed using the method within a 4.5 Å radius of the residues.

peritonitis. Compared to the normal group, IL-6 levels significantly increased post-MDP induction, indicating activation of downstream inflammatory pathways (Fig. 6A). The IL-6 levels in the **RP20**-treated groups were significantly and dose-dependently reduced compared to the model group. This suggests that **RP20** effectively inhibits RIPK2 activity *in vivo*, blocking downstream inflammatory signals and subsequently affecting the synthesis and release of the cytokine IL-6.

Subsequently, we established an APAP-induced ALI model to assess the anti-inflammatory and hepatoprotective effects of compound **RP20**. As shown in Fig. 6B and C and Supporting Information Fig. S8, **RP20** markedly diminished alanine transaminase (ALT) and aspartate aminotransferase (AST) levels, and reduced liver necrosis. The reduction in serum levels of TNF-α, IL-1β, and IL-6 (Fig. 6D) correlated with corresponding liver mRNA levels, showcasing **RP20**'s substantial impact on inflammatory factors. Notably, **RP20** attenuated inflammatory mediators in serum by downregulating liver mRNA levels, emerging as a key contributor to ALI alleviation and therapeutic intervention (Fig. 6E). Additionally, **RP20** demonstrated dose-dependent hepatoprotective effects by enhancing GSH production in liver tissue, surpassing the efficacy of **GSK2983559** at an equimolar dosage (Fig. 6F).

To further elucidate the mechanism of **RP20** in ALI, we employed TUNEL assays and Western blotting to assess liver apoptosis and the expression levels of relevant proteins in hepatic tissues. As illustrated in Fig. 7A and B, **RP20** demonstrated dose-dependent hepatoprotective effects, surpassing the efficacy of **GSK2983559** at an equimolar dosage. **RP20** significantly downregulated the levels of p-JNK, p-ERK (MAPK signaling pathways), and p-p65 (NF-κB signaling pathways) in hepatic tissues (Fig. 7C). After a single oral administration of **RP20** at a dose of 20 mg/kg, its distribution and pharmacokinetics in mice with ALI were analyzed (Fig. 7D). Remarkably, **RP20** achieved a high concentration in liver tissue, peaking at 2 h and maintaining elevated levels for up to 8 h. Serum samples were collected at various time points to assess ALT and AST levels. Following APAP induction, ALT and AST levels in the model group progressively increased, reaching 6250.74 ± 635.86 U/L and 6749.34 ± 765.41 U/L at 8 h, respectively (Fig. 7E). In contrast, ALT and AST levels in the **RP20**-treated group remained consistently low, indicating a significant hepatoprotective effect. Additionally, serum levels of inflammatory cytokines TNF-α, IL-1β, and IL-6 were measured over time (Fig. 7F). IL-1β and IL-6 levels began to rise 4 h post-induction, while TNFα levels increased at 8 h. Compared to the model group, **RP20** treatment significantly reduced TNF-α and IL-1β levels, with a notable decrease in IL-6 as well. These findings suggest that **RP20** exhibits strong liver-targeting properties, maintaining high concentrations in liver tissue and demonstrating potent anti-inflammatory and hepatoprotective effects.

Under a lethal dosage, all mice in the APAP model group died within 66 h. However, treatment with **RP20** and **GSK2983559** could significantly prolong the survival of mice (Fig. 7G). Remarkably, all mice in the group treated with 20 mg/kg **RP20** survived, while NAC only deferred the time of mortality without conferring a significant enhancement in overall survival. Orally administered at a dosage of 20 mg/kg, **RP20** facilitated a gradual return of body temperature to normal levels 12 h after post-APAP induction (Fig. 7H).

3. Discussions

RIPK2 is highly expressed in various cancers, including breast, colorectal, and ovarian cancers, with particularly strong associations in clear cell renal cell carcinoma, where its elevated expression correlates with advanced clinical stages and metastasis[38-40]. RIPK2 also demonstrates oncogenic potential in prostate cancer metastasis, pancreatic cancer, and glioblastoma multiforme[41-43]. Notably, in inflammatory breast cancer (IBC), where "molecular inflammation" drives tumor progression and metastasis, RIPK2 inhibitors may serve as promising therapeutic strategies[44]. Beyond its role in cancer, RIPK2 is involved in regulating multiple inflammatory and immune diseases, such as asthma, inflammatory bowel disease, and rheumatoid arthritis. It

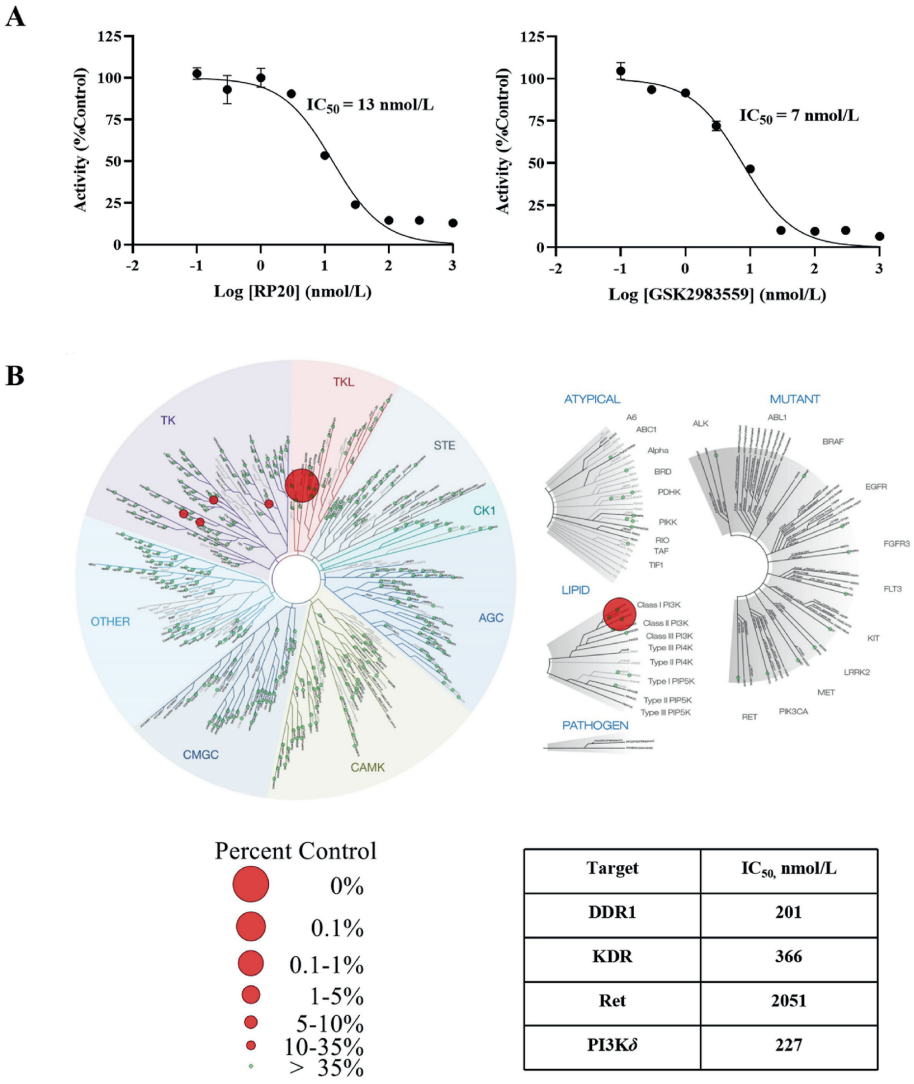

Target	IC_{50}, nmol/L
DDR1	201
KDR	366
Ret	2051
PI3Kδ	227

Figure 5 **RP20** is a selective inhibitor of RIPK2. (A) The dose−response curves of compound **RP20** and **GSK2983559** against RIPK2. (B) The kinase selectivity evaluation of compound **RP20** at a concentration of 1 μmol/L at Eurofins.

also plays a pivotal role in autoimmune diseases like Behcet's disease and systemic lupus erythematosus, as well as in neuro-inflammatory conditions like stroke, Alzheimer's disease, and multiple sclerosis[45-47]. Given its involvement in both cancers and immune-related diseases, RIPK2 inhibitors, such as **RP20**, hold significant potential for diverse clinical applications.

Meanwhile, there are still some limitations in this study. Firstly, this research focuses on the pharmacodynamic effects of RIPK2 inhibitors in APAP-induced ALI and preliminarily explores potential mechanisms. However, an in-depth analysis of key proteins expression in relevant signaling pathways has not been conducted, which will be a primary focus of future studies. Currently, clinical research on RIPK2 inhibitors is predominantly directed toward the treatment of inflammatory bowel diseases, and the relationship between the disease and the target has been well-established. In contrast, the application of RIPK2 inhibitors for the treatment of ALI is an innovative direction first proposed by our team. In future clinical studies, we may face challenges, such as the unknown therapeutic sensitivity of **RP20** in liver injury caused by multiple factors. This remains a critical issue for further investigation. Notably, although compounds OD101 and AC-101 have progressed to clinical stages, their chemical structures, detailed clinical outcomes, and potential limitations have not been publicly disclosed. As a result, we are unable to definitively assert that **RP20** is a superior RIPK2 inhibitor compared to these compounds.

It is undeniable that CMD-OPT offers significant advantages in drug development by leveraging a user-friendly transformer-based framework for molecular optimization. By enabling scaffold hopping and refining pharmacokinetic properties, CMD-OPT overcomes the limitations of parent molecules like **GSK2983559**. It addresses the challenge of making artificial intelligence (AI) models more practical for drug design by constraining the molecular generation space with multiple conditions. This approach may significantly enhance the applicability of AI models in the drug design field, facilitating their effective implementation and improving their overall utility.

4. Conclusions

ALI represents a serious hepatic disorder with limited clinically available treatments. This study introduces CMD-OPT, a two-

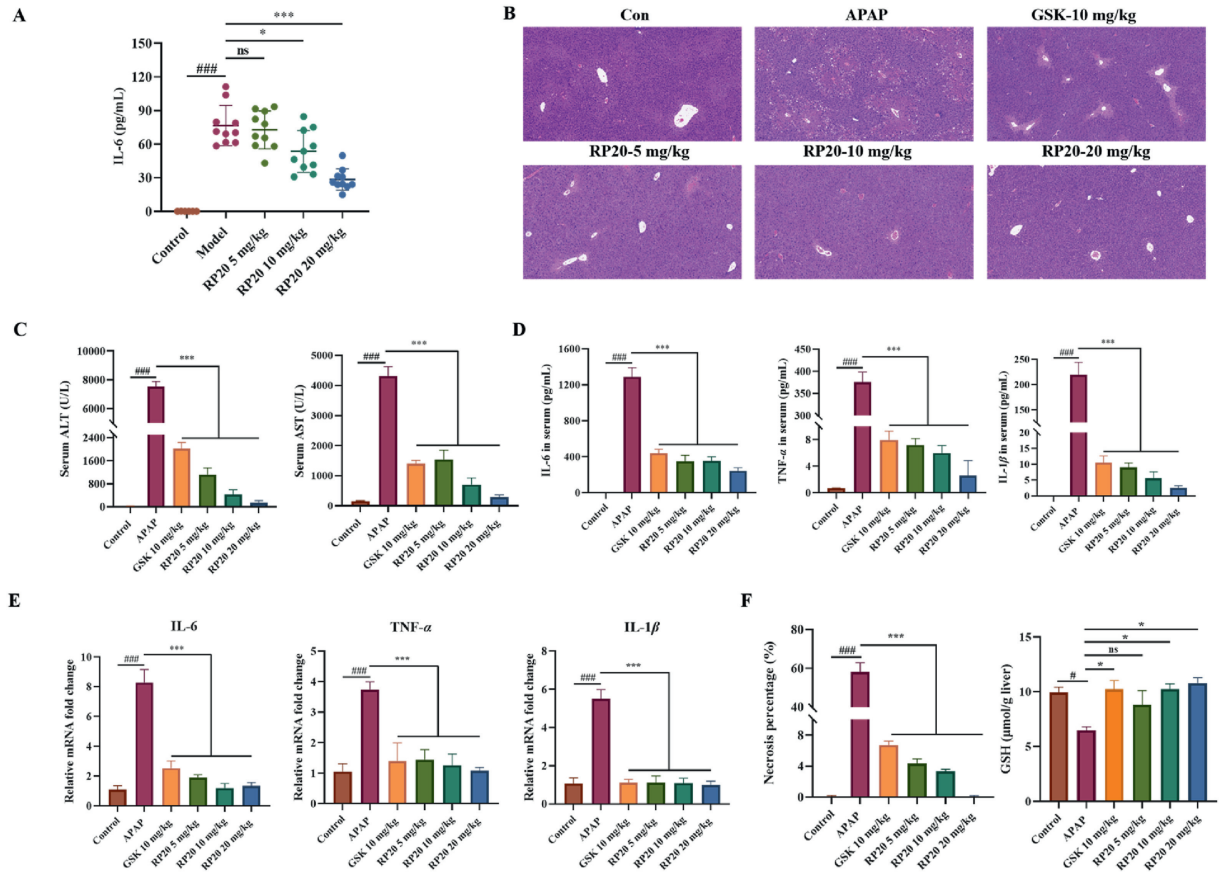

Figure 6 **RP20** inhibits NOD2 signaling *in vivo* and has a beneficial effect on an ALI model. (A) Pharmacodynamic study of **RP20** on MDP induced peritonitis model in C57BL/6 mice. 8-week female C57BL/6 mice were sacrificed after 4 h of MDP (100 μg/piece) induction and the serum were obtained. IL-6 levels in serum using ELISA kits. $n = 10$ (Control, $n = 6$), mean ± SD. (B) Effects of **RP20** and **GSK2983559** on APAP-induced ALI model. 6−8 weeks C57BL/6 mice were sacrificed after 12 h of APAP (500 mg/kg) induction and the liver tissues were obtained. H&E staining after fixation with 10% paraformaldehyde. Scale bar, 100 μm. (C) ALT and AST levels by blood biochemical analyzer; $n = 6$, mean ± SD. (D, E) TNF-α, IL-1β and IL-6 levels in serum using ELISA kits. $n = 3$, mean ± SD; TNF-α, IL-1β and IL-6 mRNA levels in the liver were detected by QPCR. (F) Statistical chart of liver necrosis area; detection of GSH level in liver tissue using T-GSH kit. $n = 3$, mean ± SD. Compared with the control group, $^{\#}P < 0.05$, $^{\#\#\#}P < 0.001$; compared with the APAP model group, $^{*}P < 0.05$, $^{***}P < 0.001$; ns means no significant difference.

stage molecular optimization tool centered on a known active lead compound, to synthesize a series of potent RIPK2 inhibitors exemplified by compound **RP20**. **RP20** demonstrated exceptional kinase selectivity, favorable oral pharmacokinetics, and superior therapeutic efficacy in an APAP-induced ALI model. Data indicate that **GSK2983559** exhibited a non-linear dose−response in high-dose safety studies in rats, which impeded a comprehensive toxicological assessment at the highest doses. This issue may be a primary reason for its failure in clinical safety evaluations, although detailed explanations were not provided. In contrast, **RP20** successfully passed all rigorous tests in the Safety47 panel, and a sequential 28-day *in vivo* study demonstrated the compound's favorable oral safety profile. Additionally, **RP20** exhibited significantly lower inhibitory activity on the major CYP450 isoforms, CYP3A4 and CYP2D6, compared to **GSK2983559** (Supporting Information Table S9). Therefore, we hypothesize that **RP20** may offer superior clinical safety.

Moreover, preclinical pharmacodynamic studies for the treatment of DSS-induced acute ulcerative colitis are underway. At equivalent doses, oral **RP20** administration demonstrates superior efficacy compared to **GSK2983559**, significantly reducing disease scores and markedly improving the survival and body weight of mice (Supporting Information Fig. S9). Pharmacodynamic studies on **RP20** for the treatment of multiple sclerosis and in combination with PD-L1 for the treatment of pancreatic cancer are also in progress. These findings highlight **RP20** as a promising preclinical candidate poised for advancement into clinical trials. Importantly, this study marks the first use of RIPK2 inhibitors for ALI treatment, opening a novel therapeutic avenue for clinical applications.

5. Experimental

5.1. *Chemistry*

We used commercially available solvents and reagents without additional purification. Reactions were monitored using TLC. For key intermediate and final products preparation, we employed a Biotage automatic purification system with purity confirmed to be >95% *via* an Agilent ZORBAX SB-C18 reversed-phase column.

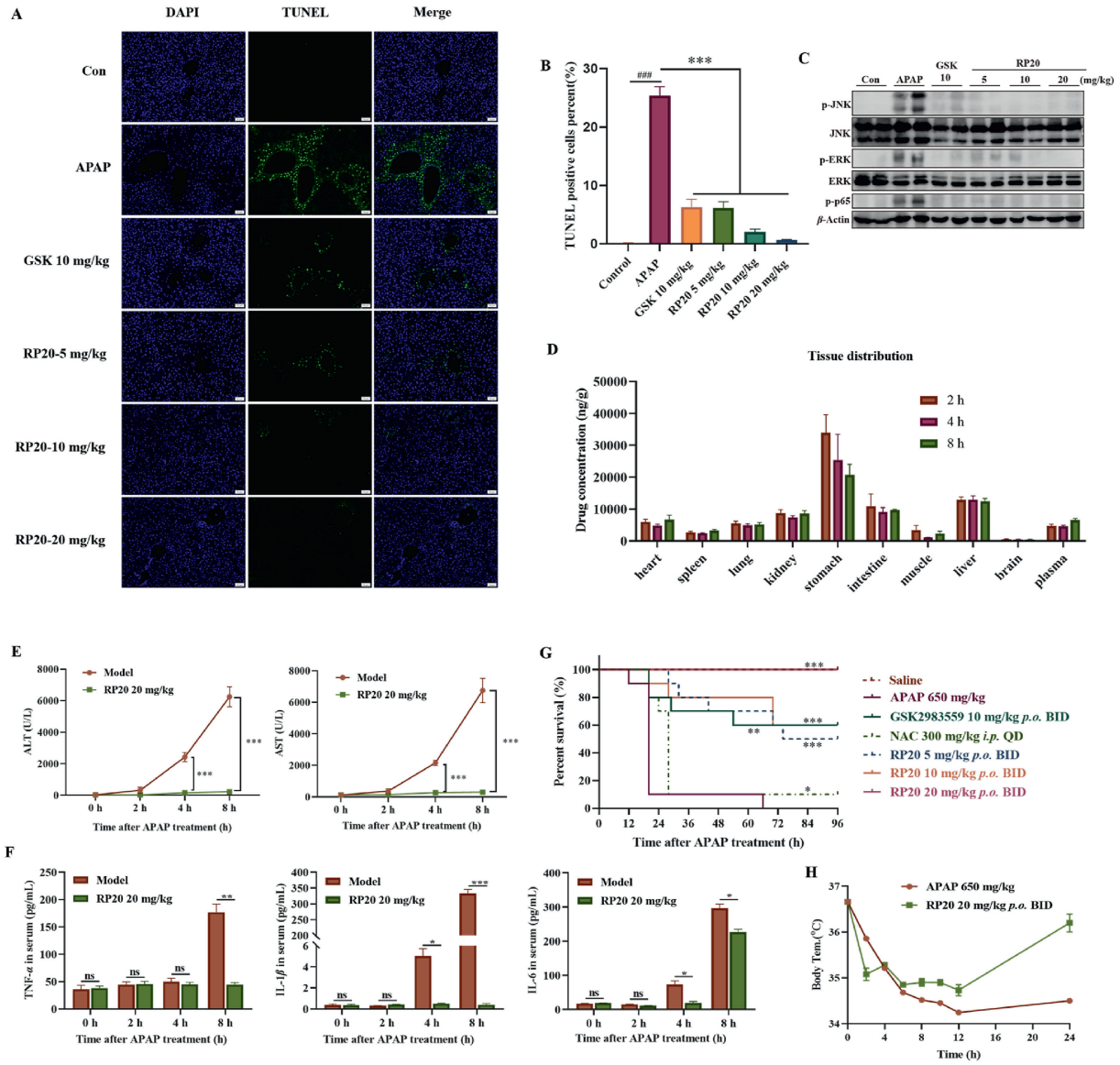

Figure 7 **RP20** has hepatoprotective effects on ALI models and exhibits liver-targeting properties. (A) TUNEL immunohistochemical staining of liver cells across various experimental groups. Scale bar, 50 μm. (B) Liver cell apoptosis statistics. $n = 3$, mean ± SD. (C) **RP20** inhibits NF-κB and MAPK (p-JNK, p-ERK, p-p65) in liver tissues from treatment groups. (D) Tissue distribution of **RP20** in mice with ALI. 6−8 weeks C57BL/6 mice were sacrificed after 2, 4, 8 h after APAP (500 mg/kg) induction and the serum were obtained. $n = 5$, mean ± SD. (E) ALT and AST levels by blood biochemical analyzer; $n = 5$, mean ± SD. (F) TNF-α, IL-1β and IL-6 levels in serum using ELISA kits. $n = 2$, mean ± SD. (G) Survival of mice with ALI induced by ultra-high dose APAP ($n = 10$). (H) Body temperature change of model and **RP20**-20 mg/kg groups. In comparison to the control, $^{\#\#\#}P < 0.001$; compared with the APAP model group, $^{*}P < 0.05$, $^{**}P < 0.01$, $^{***}P < 0.001$; ns means no significant difference.

Mass analysis was conducted using a Waters SQD2 single quadrupole mass detection system with electrospray ionization (ESI) source. ^{1}H NMR and ^{13}C NMR spectra were recorded on a BRUKER AVANCE II 400 MHz spectrometer, and chemical shifts were reported in parts per million (ppm) with TMS as the internal standard. Coupling constants are reported in Hz, and multiplicities are indicated as singlet (s), doublet (d), triplet (t), quartet (q), or multiplet (m). Firstly, intermediate **12** was prepared using the following synthesis route (5-step reaction) as shown in Scheme 3.

5.1.1. Preparation of N-(2-fluoro-5-nitrophenyl)benzamide

Dissolve 15.6 g (100 mmol) of 2-fluoro-5-nitroaniline in 200 mL of acetonitrile and add benzoyl chloride (12.8 mL, 110 mol) in portions. Heat to 50 °C and allow to react for 4 h. A significant amount of solid precipitates in the system. Filter the mixture, and the resulting cake is washed with acetonitrile to obtain a relatively pure intermediate. ^{1}H NMR (400 MHz, DMSO-d_6) δ 10.51 (s, 1H), 8.67 (dd, $J = 6.5, 2.9$ Hz, 1H), 8.17 (ddd, $J = 9.1, 4.1, 2.9$ Hz, 1H), 8.03−7.97 (m, 2H), 7.69−7.53 (m, 4H).

5.1.2. Preparation of N-(5-amino-2-fluorophenyl)benzamide

Mix the intermediate obtained from the previous step (22.1 g, 85 mmol) with iron powder (9.5 g, 170 mmol) and ammonium chloride (9.1 g, 170 mmol) in a solvent mixture of methanol/water (4:1) and heat to 65 °C. After 1 h, verify reaction completion through TLC. Filter the suspension through diatomaceous earth,

retaining the mother liquor. Concentrate the mother liquor, disperse it in 100 mL of water for slurry formation, and filter to obtain a relatively pure intermediate. ^{1}H NMR (400 MHz, DMSO-d_6) δ 9.86 (s, 1H), 7.95 (d, J = 7.5 Hz, 2H), 7.65−7.48 (m, 3H), 6.93 (t, J = 9.6 Hz, 1H), 6.81 (dd, J = 6.7, 2.8 Hz, 1H), 6.49−6.38 (m, 1H), 5.02 (s, 2H).

5.1.3. Preparation of N-(2-amino-6-fluorobenzo[d]thiazol-5-yl) benzamide

Combine the intermediate from the previous step (13.8 g, 60 mmol) with KSCN (8.75 g, 90 mmol) in 100 mL of acetic acid. Gradually add an acetic acid solution containing Br_2 (4.5 mL, 90 mmol) to the system. After 5 h, a significant amount of solid precipitates. Filter the mixture to obtain a relatively pure intermediate. ^{1}H NMR (400 MHz, DMSO-d_6) δ 10.16 (s, 1H), 8.66 (s, 2H), 7.99−7.91 (m, 2H), 7.78 (d, J = 9.9 Hz, 1H), 7.66 (d, J = 6.5 Hz, 1H), 7.61−7.55 (m, 1H), 7.51 (t, J = 7.5 Hz, 2H).

5.1.4. Preparation of N-(6-fluorobenzo[d]thiazol-5-yl) benzamide

Dissolve the intermediate from the previous step (14.3 g, 50 mmol) in 150 mL of tetrahydrofuran under ice bath conditions. Add isoamyl nitrite (10 mL, 75 mmol) dropwise. After the addition, allow the reaction to continue at room temperature for 2 h, resulting in a significant amount of solid precipitation. Filter the mixture to obtain a relatively pure intermediate. ^{1}H NMR (400 MHz, DMSO-d_6) δ 10.39 (s, 1H), 9.41 (s, 1H), 8.32 (d, J = 6.8 Hz, 1H), 8.19 (d, J = 10.0 Hz, 1H), 8.03 (dd, J = 7.2, 1.8 Hz, 2H), 7.63 (t, J = 7.3 Hz, 1H), 7.56 (dd, J = 8.2, 6.7 Hz, 2H).

*5.1.5. Preparation of 6-fluorobenzo[d]thiazol-5-amine (intermediate **12**)*

Dissolve the intermediate from the previous step (10.9 g, 40 mmol) in 70% concentrated sulfuric acid (100 mL) and heat to 100 °C. After 4 h of reaction, confirm completion through TLC. Cool the reaction mixture to room temperature and slowly dilute it into ice water. Adjust the pH to above 10 using sodium hydroxide. Then, extract the mixture twice with 500 mL of ethyl acetate, combine the organic phases, and concentrate. Disperse the concentrated crude product in 100 mL of ether, filter it, and obtain a relatively pure product. ^{1}H NMR (400 MHz, DMSO-d_6) δ 9.13 (s, 1H), 7.77 (d, J = 10.9 Hz, 1H), 7.35 (dd, J = 8.2, 1.1 Hz, 1H), 5.35 (s, 3H). Then, synthesis method and structural characterization of the compound **RP1** using the following synthesis route as shown in Scheme 4**.**

*5.1.6. Preparation of 6-bromo-N-(6-fluorobenzo[d]thiazol-5-yl) thieno[2,3-d]pyrimidin-4-amine (intermediate **13**)*

A mixture of starting materials **11** (25 g, 100 mmol), intermediate **12** (16.8 g, 110 mmol), and *p*-toluenesulfonic acid (1.7 g, 10 mmol) was added to a 500 mL round-bottom flask, and isopropanol (250 mL) was added. The temperature was set at 80 °C. After 2 h, the reaction was confirmed to be complete by TLC, and a significant amount of solid precipitated. After filtration, the cake was washed with ether to obtain a high-purity intermediate **13**. ^{1}H NMR (400 MHz, DMSO-d_6) δ 10.26 (s, 1H), 9.39 (s, 1H), 8.40 (d, J = 1.2 Hz, 1H), 8.26 (d, J = 6.8 Hz, 1H), 8.18 (d, J = 9.9 Hz, 1H), 8.14 (s, 1H).

*5.1.7. Preparation of tert-butyl 4-(4-((6-fluorobenzo[d]thiazol-5-yl)amino)thieno[2,3-d]pyrimidin-6-yl)-3,6-dihydropyridine-1(2H)-carboxylate (intermediate **14a**)*

The previously obtained intermediate **13** (19.1 g, 50 mmol), *N-Boc*-1,2,5,6-tetrahydro-4-boronol-pyridinyl ester (17 g, 55 mmol), potassium carbonate (13.8 g, 100 mmol), and $PdCl_2$ (dppf) (1.8 g, 2.5 mmol) were added to a 500 mL three-neck flask. A solvent mixture of dioxane/ethanol/water (7:3:4, total 200 mL) was added, and the reaction was conducted at 80 °C after purging with nitrogen three times. After 2 h, a significant amount of solid precipitated, and it was filtered. The cake was washed with a small amount of ethanol to obtain a high-purity intermediate **14a**. ^{1}H NMR (400 MHz, DMSO-d_6) δ 9.81 (s, 1H), 9.40 (s, 1H), 8.40 (s, 1H), 8.36 (dd, J = 7.4, 2.6 Hz, 1H), 8.20 (d, J = 9.8 Hz, 1H), 7.82 (d, J = 5.5 Hz, 1H), 6.22 (s, 1H), 4.10−3.96 (m, 2H), 3.59 (m, 2H), 2.62−2.51 (m, 2H), 1.45 (s, 9H).

*5.1.8. Preparation of N-(6-fluorobenzo[d]thiazol-5-yl)-6-(1,2,3,6-tetrahydropyridin-4-yl)thieno[2,3-d]pyrimidin-4-amine (**RP1**)*

The intermediate **14a** from the previous step (11.6 g, 25 mmol) was dissolved in 100 mL of dichloromethane and trifluoroacetic acid (50 mL) was added in portions. After 0.5 h at room temperature, the reaction was complete, and the reaction mixture was concentrated. The concentrated solution was dispersed in water, and potassium hydroxide was added to adjust the pH to above 9, resulting in a significant amount of solid precipitation. After filtration, the cake was washed with ether to obtain the high-purity final product **RP1** without further purification. ^{1}H NMR (400 MHz, DMSO-d_6) δ 9.74 (s, 1H), 9.41 (s, 1H), 8.39−8.34 (m, 2H), 8.21 (d, J = 10.0 Hz, 1H), 7.76 (s, 1H), 6.32−6.27 (m, 1H), 3.41 (d, J = 3.1 Hz, 3H), 2.96 (t, J = 5.6 Hz, 2H), 2.44 (dq, J = 6.1, 3.4 Hz, 2H). ^{13}C NMR (101 MHz, DMSO-d_6) δ 165.73, 157.49, 155.33, 155.18 (d, J = 247.2 Hz), 153.83, 150.17, 142.10, 131.49 (d, J = 11.2 Hz), 130.07, 127.82, 126.06 (d, J = 15.3 Hz), 121.20, 118.02, 113.91, 109.39 (d, J = 26.4 Hz), 45.35, 42.75, 27.30. HRMS-ESI: Calcd. for $C_{18}H_{15}FN_5S_2$: 384.0747[M+H]$^+$, found: 384.0735. Last, the synthesis and characterization data for other compounds are detailed in the Supporting Information

5.2. Biological methods

5.2.1. RIPK2/1 kinase assay

The kinase enzymatic inhibition assay was carried out in Eurofins Discovery (Cerep, France). RIPK2 (h) is incubated with 20 mmol/L Tris/HCl pH 8.5 (RIPK1, 8 mmol/L MOPS pH 7.0), 0.2 mmol/L EDTA, 0.33 mg/mL myelin basic protein, 10 mmol/L Magnesium acetate and [γ-^{33}P-ATP] (specific activity and concentration as required). The reaction is initiated by the addition of the Mg/ATP mix. After incubation for 120 min at room temperature, the reaction is stopped by the addition of phosphoric acid to a concentration of 0.5%. 10 μL of the stopped reaction is spotted onto a P30 filtermat and washed four times for 4 min in 0.425% phosphoric acid and once in methanol prior to drying and scintillation counting.

5.2.2. Metabolic stability assay in human liver microsome

The *in vitro* metabolic stability assessment was performed using pooled liver microsomal fractions, maintaining a final protein concentration of 0.5 mg/mL and a test compound concentration of 1 μmol/L. The reaction began upon adding an NADPH-regenerating system. At different time intervals, 100 μL samples

of the reaction mixture were collected and added to plates with a quenching solution. LC−MS/MS analysis was used to measure the test compound concentration in the samples. The predicted clearance was estimated using the well-stirred liver model, without considering protein binding.

5.2.3. Plasma exposure tests for selected compounds

The selected compounds were prepared in a saline solution containing 2.5% DMSO and administered to BALB/c mice ($n = 3$) by oral administration at a dosage of 10 mg/kg. Blood samples were drawn at specified intervals of 0.5, 2, and 6 h post-dosing and centrifuged to isolate the plasma. The plasma samples were treated with acetonitrile, which included an internal standard (SAHA), for protein precipitation. After an additional centrifugation step, the concentrations of the compounds in the supernatant were measured using LC−MS/MS. The primary pharmacokinetic parameters were determined and are provided in Table S2.

5.2.4. Pharmacokinetic study

The compounds were prepared in a saline solution with 2.5% DMSO and administered to mice (or SD rats) ($n = 4$) *via* both intravenous injection and oral administration at a dosage of 10 mg/kg. Blood samples were taken at predetermined intervals: 5 and 15 min, 0.5, 1, 2, 4, 6, 8, 10, 24, and 48 h post-dosing. The samples were centrifuged to separate the plasma. Plasma proteins were precipitated using acetonitrile with an internal standard (SAHA). Following a second centrifugation, the concentrations of the compounds in the supernatant were quantified through LC−MS/MS. The pharmacokinetic parameters were calculated and presented in Table S3.

5.2.5. Induction of THP-1 and BMDM cells with L18-MDP

THP-1 and BMDM cells were plated at a density of 5×10^5 cells/mL in 2 mL of medium in 6-well plates and incubated overnight in a cell culture incubator. The next day, the cells were pre-treated with 2 μmol/L RP20 for 30 min before being stimulated with 200 ng/mL L18-MDP to induce cell activation. Cell lysates were collected at specified time points for further analysis of intracellular protein expression levels using Western blotting. The antibodies used were human RIPK2 antibody (Santa Cruz, sc-166765, 1:500), human p-JNK(Thr183/Ser185) antibody (Cell Signaling Technologies, 4668T, 1:1000), human JNK mAb (Zenbio, R22866, 1:1000), human phospho-p38 (T180/Y182) rabbit mAb (abcam, ab195049, 1:1000), human p-38 antibody (abcam, ab170099,1:1000), human p-p65 antibody (Zenbio, 310013, 1:1000), human IκBα antibody (Zenbio, 380682, 1:1000), and β-actin (Abways, AB2001, 1:5000).

5.2.6. Protein expression and purification

The cDNA of human RIPK2 containing residues 1−310 were cloned into the pFastBacHT plasmid. A 10X histidine tag and TEV cleavage site was added to the N-terminal of the RIPK2. Bacmids were generated in DH10Bac™ cells, and the resulting baculoviruses were generated and amplified in Sf9 insect cells. After infection by Bac-to-Bac baculoviruses for 48 h, the cells were harvested in a lysis buffer containing 20 mmol/L Tris (pH 7.5), 500 mmol/L NaCl, 5% glycerol, 2 mmol/L β-Me, 1 mmol/L TCEP and cocktail. The expressed protein was purified by a Ni-NTA column (QIAGEN) and transformed into the lysis buffer containing TEV protease for removing the additional residues. The resulting protein sample was further passed through the Ni-NTA column followed by a S200 size-exclusion chromatography (GE Healthcare) with a solution containing 20 mmol/L Tris (pH 8.0), 150 mmol/L NaCl, 5% glycerol and 1 mmol/L TCEP. The purified RIPK2 protein was concentrated to 10 mg/mL and flash frozen for storage at −80 °C.

5.2.7. Protein crystallization and co-crystal structure determination

Apo RIPK2 crystals were obtained by the hanging drop method using 1 μL of 10 mg/mL RIPK2 and 1 μL 0.1 mol/L Mes pH 6.0, 0.25 mol/L $CaCl_2$, 3% ethanol, and 5% PEG 1000 at 20 °C. The crystals were soaked with 0.1 μL of 100 mmol/L RP20 (dissolved in DMSO) for 12 h. The crystals were rapidly frozen in liquid nitrogen using a reservoir solution containing 20% glycerol as a cryoprotectant. X-ray diffraction data were gathered at beamline BL19U of the Shanghai Synchrotron Radiation Facility. The data processing was carried out using the HKL3000 software suite. Molecular replacement was performed with CCP4i software, using a model based on PDB entry 4C8B. Model building was done in Coot, while refinement involved reciprocal-space adjustments, individual B factors, TLS parameters, and occupancies using PHENIX. The finalized structures have been submitted to the Protein Data Bank, with accession numbers provided in Table S6, along with detailed statistics and quality assessments of the structures.

5.2.8. Kinase selectivity evaluation at Eurofins

RP20 was evaluated for its activity against a set of 373 kinases using the KinaseProfile™ assay at Eurofins (Cerep, France). A chosen inhibitor for each specific kinase is added to each plate in duplicate at a concentration known to result in complete inhibition. This generates the blank wells. For kinases where no known inhibitor exists, 30% phosphoric acid will replace the inhibitor blank. A full list of the kinases is shown in Table S7 and data is represented at percent control (% Ctrl). RIPK2 was 100% inhibited by RP20 at 1 μmol/L. More details about the KinaseProfile™ and protocols are available at https://www.eurofinsdiscovery.com.

5.2.9. In vitro safety evaluation of RP20

Safety47™ panel was provided by Discover X (USA) against 78 assays in the SAFETYscan EC/IC_{50} ELECT service. The assays employed PathHunter enzyme fragment complementation (EFC) technology, FLIPR®-based cell assays, KINOMEscan kinase binding evaluations, along with several enzymatic tests (Table S7).

5.2.10. CYP450 inhibitory activity evaluation

All incubations were performed at 37 °C with shaking, using three replicates ($n = 3$) for each experimental group. The incubation mixtures were prepared in 100 mmol/L potassium phosphate buffer (pH 7.40 ± 0.10) and included microsomes (0.5 mg protein/mL), **RP20**, and **GSK2983559** at concentrations of 0.01, 0.1, 1, 10, and 100 μmol/L, along with CYP isozyme-selective substrates (dextromethorphan for CYP2D6 and testosterone for CYP3A4). After a 5-min pre-incubation, the reaction was initiated by adding an NADPH-regenerating system. The CYP3A4-testosterone reaction proceeded for 5 min, while the CYP2D6 reaction lasted for 30 min. At the end of each incubation period, the reactions were stopped by adding 200 μL of acetonitrile containing the internal standard. The mixtures were then centrifuged at 16,200×g for 10 min, and the supernatants were subjected to LC−MS/MS analysis.

5.2.11. Source of animals

BALB/c mice, weighing 20−22 g each, and SD rats, weighing 200−250 g each, were obtained from Chengdu Dossy Experimental Animals Co., Ltd. (Chengdu, China). Male C57BL/6 mice, aged 6−8 weeks and weighing approximately 22−25 g, were procured from Beijing Huafu Kang Biological Technology Co., Ltd. (Beijing, China). The mice were housed in groups of five per cage in the SPF-grade Huaxi Animal Center at Sichuan University's National Key Laboratory of Biomedicine. They were provided with sterile water and autoclaved rodent maintenance feed, allowing *ad libitum* access to both food and water. The environmental conditions in the facility were maintained at a stable temperature of 22 ± 2 °C, a relative humidity of 55%, and a 12 h light−dark cycle from 8:00 AM to 8:00 PM. To acclimate to the environment, the mice were housed for approximately one week before conducting the relevant experiments. All animal husbandry and experimental procedures strictly adhered to the guidelines established by the Animal Management Committee of Sichuan University.

5.2.12. MDP-induced peritonitis model

Eight-week-old female C57BL/6 mice were acclimated for one week prior to the experiment. The mice were then randomly assigned to the control group, model group, and treatment groups (receiving low, medium, or high doses of **RP20**). Thirty minutes after oral administration of either the vehicle or **RP20**, the mice were given an intraperitoneal injection of PBS or 100 μg of MDP. Four hours post-MDP administration, the mice were euthanized by CO_2 asphyxiation, followed by blood collection *via* cardiac puncture. In our study, euthanasia was conducted according to the national standard GB/T 39760−2021, Guidelines for the Euthanasia of Laboratory Animals, which lists CO_2 as a recommended method for rodents when administered in a gradual and controlled manner. The procedure was approved by the institutional animal ethics committee, and the use of CO_2 complies with both regulatory and ethical standards. We utilized a fully automated CO_2 euthanasia system (Model FSZZ-2A), which ensures a gradual fill rate of 10%−30% chamber volume per minute, as recommended. The transparent design allowed constant observation of the animals, and the euthanasia was conducted by trained personnel in a ventilated room. No abnormal behaviors (*e.g.*, gasping, vocalization, seizure-like movements) were observed during the process.

*5.2.13. Efficacy evaluation of **RP20** on APAP-induced acute liver injury model*

Male C57BL/6 mice were randomly divided into the specified experimental groups: Saline group, 500 mg/kg APAP-induced group, 500 mg/kg APAP + **RP20** 5 mg/kg group, 500 mg/kg APAP + **RP20** 10 mg/kg group, 500 mg/kg APAP + **RP20** 20 mg/kg group, and 500 mg/kg APAP + **GSK2983559** 10 mg/kg group, with each group comprising five mice. Before induction, the mice were fasted for 16 h but had access to water. The 500 mg/kg APAP was administered *via* intraperitoneal injection, followed immediately by oral treatment. After 12 h of APAP induction, the mice were euthanized, and peripheral blood was collected before conducting necropsy. The liver was divided into four portions, with one piece fixed in 4% paraformaldehyde for subsequent immunohistochemistry. The remaining three portions were snap-frozen in liquid nitrogen for the extraction of tissue proteins, mRNA, and the assessment of related markers.

5.2.14. Tissue distribution detection

The ALI model was established as described above (4.2.13.). After administration at a dose of 20 mg/kg, the mice were euthanized, and peripheral blood was collected before conducting necropsy at 2, 4, and 8 h after APAP induction, and the brain, heart, liver, spleen, lung, kidney, stomach, intestine, and muscle were taken out. The tissues were grinded and mixed. To 30 μL of tissue homogenate was added 120 μL SAHA acetonitrile solution (20 ng/mL) to precipitate the protein. 80 μL supernatant was put it into a sample vial and detected. Mass spectrometry analysis gave the concentration of the drug contained in each tissue, and converted the measured concentration into a mass concentration ng/g.

5.2.15. Tissue section immunofluorescence staining

The dehydration, tissue clearing, paraffin embedding, slide preparation, embedding, sectioning, slide baking, and dewaxing steps for liver tissue followed the procedures. Subsequent to completing these steps, the tissue sections were subjected to permeabilization using Proteinase K (20 μg/mL) at 37 °C for 15 min. Following permeabilization, the sections were thoroughly washed with PBS and subsequently blocked with 2% BSA at 37 °C for 30 min. The reaction mixture for TUNEL staining was prepared according to the instructions provided with the TUNEL assay kit. Subsequently, 50 μL of the staining mixture was added to the specimens, which were then incubated in the dark at 37 °C for 1 h After incubation, the sections were washed several times with PBS, allowed to air dry, and then subjected to DAPI nuclear staining in the dark for 5 min. The slides were sealed using a mounting medium containing anti-fading agents, and panoramic tissue scans were performed using the OLYMPUS whole-slide imaging system. This protocol outlines the steps involved in performing immunofluorescence staining on tissue sections, enabling the visualization of specific cellular components and processes.

5.2.16. Evaluation of survival period in APAP-induced acute liver injury

An acute liver injury survival period model was established in male C57BL/6 mice by intraperitoneal injection of 650 mg/kg APAP. Male C57BL/6 mice, with a body weight range of 24−25 g, were randomly assigned to the following groups: Saline group, 650 mg/kg APAP-induced group, 650 mg/kg APAP + **RP20** 5 mg/kg group, 650 mg/kg APAP + **RP20** 10 mg/kg group, 650 mg/kg APAP + **RP20** 20 mg/kg group, 650 mg/kg APAP + NAC 30 mg/kg group, and 650 mg/kg APAP + **GSK2983559** 10 mg/kg group, with each group consisting of 10 mice. Before induction, the mice underwent a 16-h fasting period without restricting water intake. Following the intraperitoneal injection of 650 mg/kg APAP, immediate oral treatment was administered, and a second dose was given 12 h after the initial induction. The observation period for this model extended for 96 h, during which all mice in the model group succumbed within this timeframe. This model was used to assess the survival period in the context of APAP-induced acute liver injury and to evaluate the impact of various treatments on mouse survival within a 96-h timeframe.

Acknowledgments

This work is financially supported by the National Natural Science Foundation of China (82304282 and T2221004), the Natural

Science Foundation of Sichuan, China (2024NSFSC1733), and the 1.3.5 project for disciplines of excellence, West China Hospital, Sichuan University (ZYGD23020).

Author contributions

Yong Chen: Writing − review & editing, Writing − original draft, Data curation, Conceptualization. Xue Yuan: Writing − original draft, Validation, Methodology, Conceptualization. Wei Yan: Methodology, Formal analysis. Yurong Zou: Software, Methodology, Data curation, Conceptualization. Haoche Wei: Methodology, Formal analysis. Yuhan Wei: Methodology. Minghai Tang: Resources, Methodology. Yulian Chen: Methodology, Formal analysis. Ziyan Ma: Resources, Methodology. Tao Yang: Methodology, Formal analysis. Kongjun Liu: Methodology, Formal analysis. Baojian Xiong: Methodology. Xiuying Hu: Writing − review & editing, Supervision. Jianhong Yang: Writing − review & editing, Supervision. Lijuan Chen: Writing − review & editing, Supervision.

Conflicts of interest

The authors declare no conflicts of interest.

Appendix A. Supporting information

Supporting information to this article can be found online at https://doi.org/10.1016/j.apsb.2025.05.003.

References

1. Ghanem CI, Pérez MJ, Manautou JE, Mottino AD. Acetaminophen from liver to brain: new insights into drug pharmacological action and toxicity. *Pharmacol Res* 2016;**109**:119−31.
2. Ramachandran A, Jaeschke H. Acetaminophen hepatotoxicity. *Semin Liver Dis* 2019;**39**:221−34.
3. Chayanupatkul M, Schiano TD. Acute liver failure secondary to drug-induced liver injury. *Clin Liver Dis* 2020;**24**:75−87.
4. Shan SL, Shen ZY, Song FY. Autophagy and acetaminophen-induced hepatotoxicity. *Arch Toxicol* 2018;**92**:2153−61.
5. Lee WM. Acetaminophen (APAP) hepatotoxicity—isn't it time for APAP to go away?. *J Hepatol* 2017;**67**:1324−31.
6. Ramachandran A, Jaeschke H. Acetaminophen toxicity: novel insights into mechanisms and future perspectives. *Gene Expr* 2018;**18**:19−30.
7. McGill MR, Hinson JA. The development and hepatotoxicity of acetaminophen: reviewing over a century of progress. *Drug Metab Rev* 2020;**52**:472−500.
8. García-Román R, Francés R. Acetaminophen-induced liver damage in hepatic steatosis. *Clin Pharmacol Ther* 2020;**107**:1068−81.
9. Getachew Y, James L, Lee WM, Thiele DL, Miller BC. Susceptibility to acetaminophen (APAP) toxicity unexpectedly is decreased during acute viral hepatitis in mice. *Biochem Pharmacol* 2010;**79**:1363−71.
10. Arnold K, Xu YM, Sparkenbaugh EM, Li MM, Han XR, Zhang X, et al. Design of anti-inflammatory heparan sulfate to protect against acetaminophen-induced acute liver failure. *Sci Transl Med* 2020;**12**: eaav8075.
11. Knight TR, Ho YS, Farhood A, Jaeschke H. Peroxynitrite is a critical mediator of acetaminophen hepatotoxicity in murine livers: protection by glutathione. *J Pharmacol Exp Therapeut* 2002;**303**:468−75.
12. Jaeschke H, McGill MR, Williams CD, Ramachandran A. Current issues with acetaminophen hepatotoxicity—a clinically relevant model to test the efficacy of natural products. *Life Sci* 2011;**88**:737−45.
13. McGill MR, Sharpe MR, Williams CD, Taha M, Curry SC, Jaeschke H. The mechanism underlying acetaminophen-induced hepatotoxicity in humans and mice involves mitochondrial damage and nuclear DNA fragmentation. *J Clin Investig* 2012;**122**:1574−83.
14. Liao CC, Yu HP, Chou AH, Lee HC, Hu LM, Liu FC. Gastrodin alleviates acetaminophen-induced liver injury in a mouse model through inhibiting MAPK and enhancing Nrf2 pathways. *Inflammation* 2022; **45**:1450−62.
15. Shu GW, Qiu YH, Hao J, Fu Q, Deng XK. γ-Oryzanol alleviates acetaminophen-induced liver injury: roles of modulating AMPK/GSK3β/Nrf2 and NF-κB signaling pathways. *Food Funct* 2019;**10**:6858−72.
16. Jun JC, Cominelli F, Abbott DW. RIP2 activity in inflammatory disease and implications for novel therapeutics. *J Leukoc Biol* 2013;**94**: 927−32.
17. Jacquet S, Nishino Y, Kumphune S, Sicard P, Clark JE, Kobayashi KS, et al. The role of RIP2 in p38 MAPK activation in the stressed heart. *J Biol Chem* 2008;**283**:11964−71.
18. Hofmann SR, Girschick L, Stein R, Schulze F. Immune modulating effects of receptor interacting protein 2 (RIP2) in autoinflammation and immunity. *Clin Immunol* 2021;**223**:108648.
19. Hasegawa M, Fujimoto Y, Lucas PC, Nakano H, Fukase K, Núñez G, et al. A critical role of RICK/RIP2 polyubiquitination in Nod-induced NF-κB activation. *EMBO J* 2008;**27**:373−83.
20. Haile PA, Casillas LN, Votta BJ, Wang GZ, Charnley AK, Dong XY, et al. Discovery of a first-in-class receptor interacting protein 2 (RIP2) kinase specific clinical candidate, 2-((4-(benzo[*d*]thiazol-5-ylamino)-6-(*tert*-butylsulfonyl)quinazolin-7-yl)oxy)ethyl dihydrogen phosphate, for the treatment of inflammatory diseases. *J Med Chem* 2019;**62**: 6482−94.
21. Haile PA, Votta BJ, Marquis RW, Bury MJ, Mehlmann JF, Singhaus R, et al. The identification and pharmacological characterization of 6-(*tert*-butylsulfonyl)-*N*-(5-fluoro-1*H*-indazol-3-yl)quinolin-4-amine (GSK583), a highly potent and selective inhibitor of RIP2 kinase. *J Med Chem* 2016;**59**:4867−80.
22. Huang WS, Metcalf CA, Sundaramoorthi R, Wang YH, Zou D, Thomas RM, et al. Discovery of 3-[2-(imidazo[1,2-*b*]pyridazin-3-yl) ethynyl]-4-methyl-*N*-{4-[(4-methylpiperazin-1-yl)methyl]-3-(trifluoromethyl)phenyl}benzamide (AP24534), a potent, orally active pan-inhibitor of breakpoint cluster region-abelson (BCR-ABL) kinase including the T315I gatekeeper mutant. *J Med Chem* 2010;**53**:4701−19.
23. Nachbur U, Stafford CA, Bankovacki A, Zhan YF, Lindqvist LM, Fiil BK, et al. A RIPK2 inhibitor delays NOD signalling events yet prevents inflammatory cytokine production. *Nat Commun* 2015;**6**: 6442.
24. Sabnis RW. Novel thienopyridines as RIPK2 inhibitors for treating inflammatory bowel disease. *ACS Med Chem Lett* 2020;**11**: 2366−7.
25. Haile PA, Casillas LN, Bury MJ, Mehlmann JF, Jr SR, Charnley AK, et al. Identification of quinoline-based RIP2 kinase inhibitors with an improved therapeutic index to the hERG ion channel. *ACS Med Chem Lett* 2018;**9**:1039−44.
26. Haffner CD, Charnley AK, Aquino CJ, Casillas L, Convery MA, Cox JA, et al. Discovery of pyrazolocarboxamides as potent and selective receptor interacting protein 2 (RIP2) kinase inhibitors. *ACS Med Chem Lett* 2019;**10**:1518−23.
27. He XH, Ros SD, Nelson J, Zhu XF, Jiang T, Okram B, et al. Identification of potent and selective RIPK2 inhibitors for the treatment of inflammatory diseases. *ACS Med Chem Lett* 2017;**8**:1048−53.
28. Korashy HM, Anwar-Mohamed A, Soshilov AA, Denison MS, El-Kadi AOS. The p38 MAPK inhibitor SB203580 induces cytochrome P450 1A1 gene expression in murine and human hepatoma cell lines through ligand-dependent aryl hydrocarbon receptor activation. *Chem Res Toxicol* 2011;**24**:1540−8.
29. Yuan X, Chen Y, Tang MH, Wei YH, Shi MS, Yang YX, et al. Discovery of potent and selective receptor-interacting serine/threonine protein kinase 2 (RIPK2) inhibitors for the treatment of inflammatory bowel diseases (IBDs). *J Med Chem* 2022;**65**:9312−27.
30. Matsukiyo Y, Yamanaka C, Yamanishi Y. *De novo* generation of chemical structures of inhibitor and activator candidates for

therapeutic target proteins by a transformer-based variational autoencoder and bayesian optimization. *J Chem Inf Model* 2024;**64**: 2345−55.
31. Fu TF, Xiao C, Li XH, Glass LM, Sun JM. MIMOSA: multi-constraint molecule sampling for molecule optimization. *Proc AAAI Conf Artif Intell* 2021;**35**:125−33.
32. Wang JK, Hsieh CY, Wang MY, Wang XR, Wu ZX, Jiang DJ, et al. Multi-constraint molecular generation based on conditional transformer, knowledge distillation and reinforcement learning. *Nat Mach Intell* 2021;**3**:914−22.
33. Sun MY, Xing J, Meng H, Wang HJ, Chen B, Zhou JY. *MolSearch: search-based multi-objective molecular generation and property optimization*. KDD; 2022. p. 4724−32.
34. Polykovskiy D, Zhebrak A, Sanchez-Lengeling B, Golovanov S, Tatanov O, Belyaev S, et al. Molecular sets (MOSES): a benchmarking platform for molecular generation models. *Front Pharmacol* 2020;**11**:565644.
35. Degen J, Wegscheid-Gerlach C, Zaliani A, Rarey M. On the art of compiling and using 'drug-like' chemical fragment spaces. *ChemMedChem* 2008;**3**:1503−7.
36. Fu L, Shi SH, Yi JC, Wang NN, He YH, Wu ZX, et al. ADMETlab 3.0: an updated comprehensive online ADMET prediction platform enhanced with broader coverage, improved performance, API functionality and decision support. *Nucleic Acids Res* 2024;**52**: W422−31.
37. Damgaard RB, Nachbur U, Yabal M, Wong WW, Fiil BK, Kastirr M, et al. The ubiquitin ligase XIAP recruits LUBAC for NOD2 signaling in inflammation and innate immunity. *Mol Cell* 2012;**46**: 746−58.
38. Li DG, Tang LY, Liu B, Xu SB, Jin ML, Bo W. RIPK2 is an unfavorable prognosis marker and a potential therapeutic target in human kidney renal clear cell carcinoma. *Aging* 2021;**13**:10450−66.
39. Zhang WJ, Wang YY. Activation of RIPK2-mediated NOD1 signaling promotes proliferation and invasion of ovarian cancer cells *via* NF-κB pathway. *Histochem Cell Biol* 2022;**157**:173−82.
40. Zhang ZY, Pan Y, Zhao Y, Ren MD, Li YR, Lu GF, et al. RIPK2 promotes the progression of colon cancer by regulating BIRC3-mediated ubiquitination of IKBKG. *Exp Cell Res* 2023;**429**:113644.
41. You JQ, Wang Y, Chen HF, Jin F. RIPK2: a promising target for cancer treatment. *Front Pharmacol* 2023;**14**:1192970.
42. Sang WH, Zhou YD, Chen HY, Yu CX, Dai LS, Liu ZK, et al. Receptor-interacting protein kinase 2 is an immunotherapy target in pancreatic cancer. *Cancer Discov* 2024;**14**:326−47.
43. Yan YW, Zhou B, Qian C, Vasquez A, Kamra M, Chatterjee A, et al. Receptor-interacting protein kinase 2 (RIPK2) stabilizes c-Myc and is a therapeutic target in prostate cancer metastasis. *Nat Commun* 2022; **13**:669.
44. Zare A, Petrova A, Agoumi M, Armstrong H, Bigras G, Tonkin K, et al. RIPK2: new elements in modulating inflammatory breast cancer pathogenesis. *Cancers* 2018;**10**:184.
45. Zhao W, Leng RX, Ye DQ. RIPK2 as a promising druggable target for autoimmune diseases. *Int Immunopharmacol* 2023;**118**:110128.
46. Larochelle J, Tishko RJ, Yang CJ, Ge Y, Phan LT, Gunraj RE, et al. Receptor-interacting protein kinase 2 (RIPK2) profoundly contributes to post-stroke neuroinflammation and behavioral deficits with microglia as unique perpetrators. *J Neuroinflammation* 2023;**20**:221.
47. Xu Y, Lin F, Liao GL, Sun JX, Chen WL, Zhang L. Ripks and neuroinflammation. *Mol Neurobiol* 2024;**61**:6771−87.